Tracking the insulator-to-metal phase transition in VO_2 with few-femtosecond extreme UV transient absorption spectroscopy

Marieke F. Jager[a,1], Christian Ott[a,b,1,2], Peter M. Kraus[a], Christopher J. Kaplan[a], Winston Pouse[a,b,3], Robert E. Marvel[c,4], Richard F. Haglund[c,d], Daniel M. Neumark[a,e,5], and Stephen R. Leone[a,b,e,5]

[a]Department of Chemistry, University of California, Berkeley, CA 94720; [b]Department of Physics, University of California, Berkeley, CA 94720; [c]Interdisciplinary Materials Science Program, Vanderbilt University, Nashville, TN 37235; [d]Department of Physics and Astronomy, Vanderbilt University, Nashville, TN 37235; and [e]Chemical Sciences Division, Lawrence Berkeley National Laboratory, Berkeley, CA 94720

Contributed by Daniel M. Neumark, July 13, 2017 (sent for review May 12, 2017; reviewed by Peter Baum and Christian Spielmann)

Coulomb correlations can manifest in exotic properties in solids, but how these properties can be accessed and ultimately manipulated in real time is not well understood. The insulator-to-metal phase transition in vanadium dioxide (VO_2) is a canonical example of such correlations. Here, few-femtosecond extreme UV transient absorption spectroscopy (FXTAS) at the vanadium $M_{2,3}$ edge is used to track the insulator-to-metal phase transition in VO_2. This technique allows observation of the bulk material in real time, follows the photoexcitation process in both the insulating and metallic phases, probes the subsequent relaxation in the metallic phase, and measures the phase-transition dynamics in the insulating phase. An understanding of the VO_2 absorption spectrum in the extreme UV is developed using atomic cluster model calculations, revealing V^{3+}/d^2 character of the vanadium center. We find that the insulator-to-metal phase transition occurs on a timescale of 26 ± 6 fs and leaves the system in a long-lived excited state of the metallic phase, driven by a change in orbital occupation. Potential interpretations based on electronic screening effects and lattice dynamics are discussed. A Mott–Hubbard-type mechanism is favored, as the observed timescales and d^2 nature of the vanadium metal centers are inconsistent with a Peierls driving force. The findings provide a combined experimental and theoretical roadmap for using time-resolved extreme UV spectroscopy to investigate nonequilibrium dynamics in strongly correlated materials.

ultrafast dynamics | vanadium dioxide | insulator-to-metal transition | extreme UV

The Coulomb interaction of charges in a solid depends sensitively on local screening, bonding structure, and orbital occupancy. These electronic correlation effects are known to manifest themselves in unusual properties, such as superconductivity, colossal magnetoresistance, and insulator-to-metal phase transitions (IMTs), which can be switched on or off via small perturbations. Understanding if and how these correlation-driven properties can be manipulated in real time will open the door to using these materials as ultrafast photonic switches and will establish the electronic speed limits for next-generation devices (1–3).

Following the real-time dynamics of carrier interactions necessarily requires time-resolving the excitation and relaxation of electron correlations. Studies at longer timescales are complicated by simultaneous effects of structural distortion together with carrier screening and thermalization. In contrast, few-femtosecond extreme UV absorption spectroscopy (FXTAS) provides temporal resolution close to the Fourier limit for single-photon excitation with broadband visible light. It has the capability to separate electronic and structural effects on the basis of their intrinsic timescales and can isolate early-time electronic dynamics spectroscopically via atom-specific core-level electronic transitions (4, 5). Previous few-femtosecond and attosecond measurements of electron dynamics in solid-state systems have been restricted to simple band insulators or semiconductors and metals in which dynamics are initiated by the interaction with strong electric fields (4, 6–11). We report here on FXTAS measurements of the IMT process following single-photon excitation in vanadium dioxide (VO_2), a promising material for strongly correlated devices, and resolve the timescale of the IMT.

The insulating phase of VO_2 has monoclinic symmetry with dimerized pairs of vanadium atoms forming 1D chains within the crystal structure. As illustrated in Fig. 1, these bonds are broken and the crystal adopts a more symmetric rutile structure upon transition to the metallic phase at 340 K. The relative significance of the structural distortion in mediating the IMT has long been debated, and the driving force of the IMT in VO_2 has been described alternatively as the result of a Peierls-like structural instability, electron correlation and Mott–Hubbard effects, or a complex interplay of both (12–18). Previous time-resolved experiments on VO_2 have provided intriguing results: early optical (19, 20) and X-ray (21) measurements established subpicosecond switching times, measuring shorter and shorter timescales until an 80-fs bottleneck for the phase transition was observed in 2004 (22). However, more recent experiments in time-resolved photoemission (23) and transient reflectivity (24) have not observed the

Significance

An insulator-to-metal phase transition is a process that changes a solid material from being electrically nonconductive to being conductive. The phase transition in vanadium dioxide is a well-studied example where the process can occur in less than a picosecond, making it exciting for ultrafast electronic switches. This paper measures a record speed for the phase transition of 26 fs into a long-lived excited state of the metal that persists out to >60 ps. The extreme UV absorption spectrum of the material is also measured and (together with the ultrafast timescale) belies a structural mechanism that has long been deliberated. The measured femtosecond timescale provides fundamental insight into the electronic speed limits of these complex phenomena.

Author contributions: M.F.J., C.O., D.M.N., and S.R.L. designed research; M.F.J., C.O., P.M.K., and C.J.K. performed research; R.E.M. and R.F.H. contributed new reagents/analytic tools; M.F.J., C.O., and W.P. analyzed data; and M.F.J. wrote the paper.

Reviewers: P.B., Ludwig-Maximilians-Universität München; and C.S., Institut für Optik und Quantenelektronik Friedrich-Schiller-Universität.

The authors declare no conflict of interest.

[1]M.F.J. and C.O. contributed equally to this work.

[2]Present address: Max-Planck-Institut für Kernphysik, 69117 Heidelberg, Germany.

[3]Present address: Department of Applied Physics, Stanford University, Palo Alto, CA 94305.

[4]Present address: Thermo Fisher Scientific, Guilford, CT 06437.

[5]To whom correspondence may be addressed. Email: dneumark@berkeley.edu or srl@berkeley.edu.

This article contains supporting information online at www.pnas.org/lookup/suppl/doi:10.1073/pnas.1707602114/-/DCSupplemental.

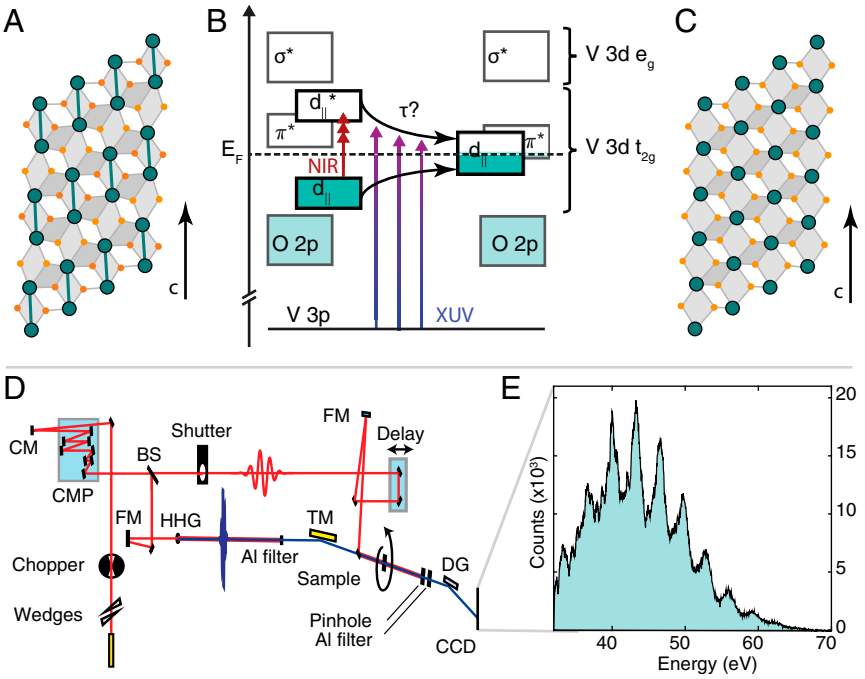

Fig. 1. (*A*) Insulating ground state of VO_2 (V atoms: gray, O atoms: orange) exhibits a monoclinic crystal structure with dimerized chains of vanadium atoms along the *c* axis and two different types of oxygen sites, those between the bonded vanadium atoms, and those between the nonbonded vanadium atoms. (*B*) Electronic structure is depicted and can be understood via crystal field theory, where the d orbitals denoted $d_{||}$ align parallel to the *c* axis of the crystal. Electrons excited across the band gap with a few-femtosecond NIR pulse initiate the IMT, and the progress is tracked via core-level transitions into the unoccupied conduction and valence band states using time-delayed attosecond pulses. (*C*) Final metallic state of the system has a rutile crystal structure in which the vanadium dimerization has been melted. (*D*) Optical layout of the experiment: CM, collimating mirror; CMP, chirped mirror compressor; BS, beam splitter; FM, focusing mirror; HHG, high harmonic generation; DG, diffraction grating. (*E*) Representative high harmonic spectrum used in the experiment, at 100-ms exposure time and 100-Hz repetition rate.

bottleneck, and measured speeds <60 fs, which were limited by the temporal resolution of the experiment. In single-crystal microrods, timescales were found to vary from 200 fs (nonpulse duration limited) to 40 fs (pulse duration limited) (25). Time-resolved electron diffraction (26, 27) has established that dilation of the V–V dimers occurs within ~300 fs, and a coherent stretching of this mode has been observed following the phase transition (22, 24, 28), but the role of electronic versus structural effects at the earliest timescales is still not well understood. The work here establishes a 26 ± 6-fs timescale for the phase transition following single-photon excitation with a few-cycle femtosecond laser pulse, not limited by the 5.6 ± 0.8-fs instrument response function measured in situ. We note that the ultrafast timescale, coupled with the finding of a d^2 ground state, is inconsistent with a structural Peierls transition, and lends support for Mott transition mechanisms.

Results

Static Extreme UV Absorption Measurements. The static extreme UV (XUV) $M_{2,3}$-edge absorption spectrum of VO_2 is measured for both the insulating and heat-induced metallic phases in transmission geometry, using attosecond pulses that cover a spectral range from 30 to 60 eV. The samples are 25-nm-thick polycrystalline thin films of VO_2 deposited on 30-nm-thick freestanding Si_3N_4 substrates, which are rapidly rotated to prevent the accumulation of heat from successive laser pulses (*Materials and Methods*). The transient evolution of this vanadium edge structure is followed in real time via FXTAS as schematically illustrated in Fig. 1. A sub-5-fs near-infrared (NIR) laser pulse centered at 760 nm impinges on VO_2 in its insulating phase, serving as the pump step to induce the IMT. Time-delayed broadband XUV attosecond pulses are then collinearly transmitted through the VO_2 thin film, probing the core-level absorption of the bulk material around the vanadium 3p transition ($M_{2,3}$ edge) at 39 eV (29). The instrument response function is monitored in situ via transient absorption of neon atoms and is measured at 5.6 ± 0.8 fs (*Neon Transient Absorption Analysis for Time-Delay Calibration*). The time-dependent changes in absorption are measured directly via changes in the optical density (ΔOD) in a NIR-pump-on/NIR-pump-off measurement. Transient absorption experiments are carried out on both the low-temperature insulating phase and the higher-temperature metallic phase of VO_2 (produced via a quartz halogen heat lamp) at an incident laser fluence of 25 mJ/cm^2, well above the fluence threshold to induce the phase transition (see ref. 26 and data in *Fluence Dependence Measurements*). The experiments on the hot metallic phase serve as a reference for the ultrafast response to interband electronic excitations and provide a direct measurement of the XUV absorption spectrum of the photoexcited metallic phase.

The measured XUV static absorption spectrum around the vanadium $M_{2,3}$ edge is shown in Fig. 2*A*, for both the insulating and metallic phases. The signal at low energies (E < 39 eV) is assigned to transitions into the continuum from the oxygen 2s core level and from the oxygen-2p–vanadium-3d hybridized valence band. This ionization-type background is fit using the signal below 35 eV, well below the onset of the vanadium M edge, with a 1/E-type form, which provided the best fit between 20 and 35 eV based on the data in the CXRO database (30). This background is subtracted across all energies to obtain the experimental $M_{2,3}$-edge spectrum shown in Fig. 2*B*.

The $M_{2,3}$-edge absorption spectrum is simulated using atomic multiplet theory, as the L- and M-edge spectra of transition metals are known to be dominated by localized atomic effects (31) and cannot be treated solely as a partial density of states of the conduction band. While consideration of formal oxidation states might suggest modeling VO_2 as a V^{4+}, or d^1, metal center, there is considerable evidence that, due to strong hybridization, the vanadium site in VO_2 is actually closer to d^2 electron occupation (13, 32–34). Indeed, it is found that the experimental $M_{2,3}$-edge spectrum is best matched with a simulated V^{3+}, or d^2, metal center. Further details of the calculations can be found in *Atomic Multiplet Simulations*. The discrete transition energies and amplitudes for the V^{3+} system are shown in Fig. 2*B*. The transition lines are multiplied by a Gaussian function (to account for the experimental energy resolution) and convoluted with a Fano lineshape (to account for final-state interference effects and lifetime broadening), generating the full M-edge spectrum, as described in *Supporting Information*. A Fano parameter of q = 2.4 provides the best fit to the data, and lies well in the range of typical Fano parameters for transition-metal M edges [q = 0.7–3.5 (35–38)]. The spectral shape of the measured core-level transition is in excellent agreement with XUV reflectivity measurements of single crystals in the same energy range (39).

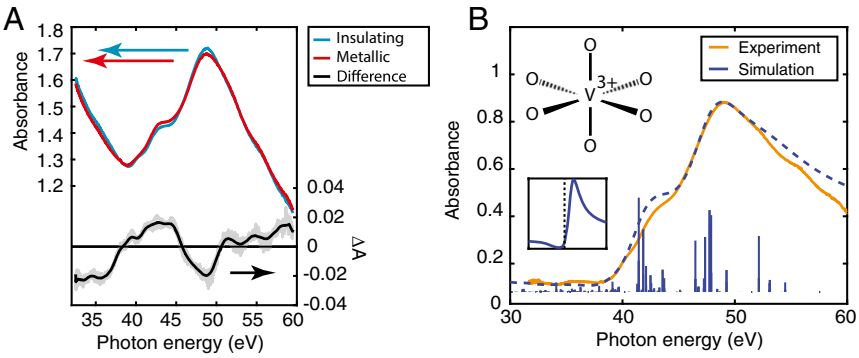

Fig. 2. (*A*) Static XUV absorbance spectra of the insulating (blue) and metallic (red) phases of VO_2 are presented on the left-hand *y* axis. The difference in absorbance (black) is shown magnified in the lower part of the figure, on the right-hand *y* axis, with error bars shown in gray. (*B*) Vanadium $M_{2,3}$ edge (orange) of the insulating phase spectrum after removing the low-energy ionization contribution. A cluster-model calculation (blue) is shown for a V^{3+} system. The transition energies and amplitudes are convoluted with the inset Fano profile to account for final-state interference effects, which maps the stick spectrum to the final simulated spectrum (blue dashed line), where due to the Fano asymmetry, spectral weight is shifted to higher energies.

XUV Transient Absorption Measurements. The time evolution of changes to the $M_{2,3}$-edge absorption spectra are shown in the FXTAS spectrograms in Fig. 3 *A* and *B*, for the metallic and insulating phases, respectively. In both cases, the system displays an abrupt response due to the initial photoexcitation and reaches a steady state within less than 100 fs, with the insulating phase equilibrating significantly faster than the metallic phase. The observed changes persist out to >60 ps (*Picosecond XUV Transient Absorption Measurements*). To compare both data sets the ΔOD changes must be plotted with respect to the same reference spectrum. The metallic phase is treated as the sum of ΔOD changes first upon heating and subsequently upon photoexcitation (i.e., as the sum of the curves in Fig. 3*C*, *Upper*) yielding the purple curve in the lower panel). This gives the cumulative ΔOD changes with respect to the insulating-phase static spectrum, which can be compared with the signal at late time delays measured in the insulating phase directly (shown as the orange curve in Fig. 3*C* (*Lower*). The two core-level spectra in the lower panel match very closely, implying the final state in each case is the same equilibrated long-lived excited state of the metallic phase. Measurements of the fluence dependence (*Fluence Dependence Measurements*) further confirm that the signal observed in the insulating phase displays a critical fluence threshold and saturation, confirming that it indeed corresponds to the phase transition.

Analysis of the Metallic Phase. The metallic-phase dynamics highlight the significant effects that carrier excitation can have on the spectrum, independent of the phase transition. The initial excitation with an NIR pulse excites dominantly ligand-to-metal charge-transfer–type transitions, which affect the allowed XUV dipole transitions and alter the shape of the spectrum. The dynamics can be globally fit with a two-component model, with an early-time spectral component corresponding to the nonequilibrium charge distribution immediately following photoexcitation and a late-time spectral component corresponding to the charge distribution following carrier–carrier and intervalley (carrier–phonon) scattering. The global fit is performed using first-order kinetics (*Global Fitting*) and the calculated spectral components and their corresponding kinetic behaviors are illustrated in Fig. 4 *A* and *B*, respectively. The tensor product of these curves gives the full 2D global fit that is shown in Fig. 3*D*. The global fit captures all of the observed dynamics and is a more rigorous way to account for broadband effects, as opposed to fitting of single lineouts. A 69 ± 11-fs time constant is obtained for the metallic phase kinetics (orange and blue curves, Fig. 4*B*).

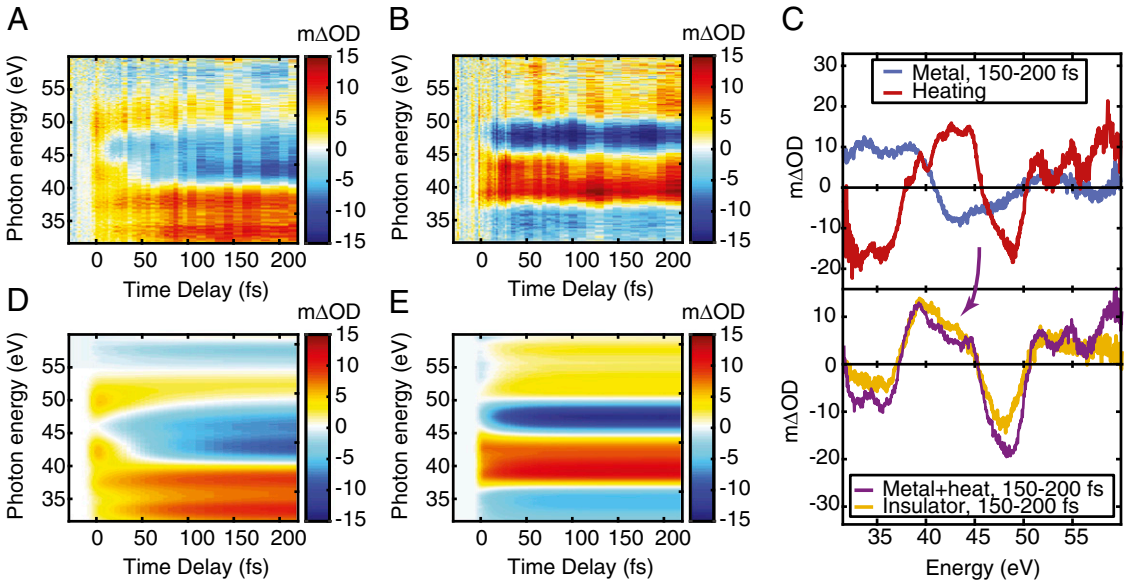

Fig. 3. Transient absorption spectrograms are shown for the metallic phase (*A*) and insulating phase (*B*) of VO_2, at an incident fluence of 25 mJ/cm^2. (*C*) Comparison of the systems at late-time delays shows that the insulator and metal reach the same final state. The metallic-phase ΔOD with respect to the insulating-phase static spectrum, shown in purple (*Lower*), is equal to the sum of the changes first upon heating (red curve, *Upper*) followed by photoexcitation (blue curve, *Upper*). Note that the red curve is identical to the difference spectrum in Fig. 2*A*. The global fits for the metallic and insulating phases are shown in *D* and *E*, respectively.

Analysis of the Insulating Phase. In the insulating phase, as in the metallic phase, the time-dependent data are well described by single-exponential kinetics. Biexponential kinetics, related to a separable observation of carrier thermalization and the IMT, are not discernible in the data. The insulating phase is thus also fit by a two-component model, which describes the evolution of an initial excitation to a final charge distribution, encompassing the IMT. The phase transition proceeds directly into an excited state of the metallic phase, as was found by the comparison at late-time delays with the photo-excited metallic phase, shown in Fig. 3*C* (*Lower*). The spectral signatures of the initial and final states of the insulator are shown in Fig. 4*C*, and the corresponding kinetics are shown in Fig. 4*D*. The time constants of both the rise and decay (Fig. 4*D*, purple and green curves) are globally fit with a value of 26 ± 6 fs. The formation of this final state represents an IMT into a long-lived excited state of the metallic phase, which persists out to more than +60 ps (*Picosecond XUV Transient Absorption Measurements*). Fluence-dependent measurements (*Fluence Dependence Measurements*) further confirm that this signal displays the characteristic threshold fluence threshold and saturation behavior associated with the phase transition.

As noted, the phase transition and carrier thermalization processes are not distinguishable in the data of the insulating phase. As described in *Global Fitting*, a three-component fit that attempts to separate these effects retrieves only one timescale for both the carrier thermalization and the insulator-to-metal transition, and no signature of the longer timescale measured in the metallic phase is discernible. This may be due to differences in the excitation step, which in the metallic phase exhibits more ligand-to-metal charge-transfer–type transitions (O 2p to V 3d bands) and the insulating phase exhibits more $\sigma \rightarrow \sigma^*$ (or $d_{||}$ to $d_{||}^*$)-type transitions, as illustrated in Fig. 1. In the final state, electrons and holes thermalize to the band edge, which has d-band character; thus this process may be apparent only in the metallic case, where the scattering processes result in a net change of oxidation state.

Discussion

The XUV measurements directly probe the electronic response of the vanadium atoms in the bulk material, establishing that the ultrafast response is not limited to the surface (23) or to single-crystal samples (25). The 26 ± 6-fs timescale observed is notably slower than the inverse plasma frequency, often associated with screening, which is calculated to be about 4 fs for the excitation density in these experiments (*Carrier Density and Plasma Frequency Estimate*). However, there is some evidence that purely electronic bottlenecks could be longer for Mott transitions (40). The electronic screening time may be a complex function of orbital-specific carrier occupation and mobility, where only a subset of the excited carriers can participate in the relevant local screening. A free-carrier screening-mediated Mott transition is schematically illustrated in Fig. 4*E*. Upon exciting an electron–hole plasma, the carriers are spatially distributed according to the oscillator strengths and joint density of states of the interband transitions. As Coulomb forces drive these carriers to new equilibrium spatial distributions the ionic vanadium sites of the lattice are progressively screened. The screened Coulomb potential (frequently described by a Yukawa potential, as illustrated in Fig. 4*E*) narrows and can reach a critical point where the d electrons, initially localized on the vanadium sites, are no longer bound and the system becomes metallic, as in a doping-driven Mott transition (41–43).

Considering a structural involvement, the 26 ± 6-fs timescale observed for the IMT is well below the 160-fs period of the A_g phonon mode previously thought to create a structural bottleneck for the phase transition (22). The fastest phonons previously hypothesized to play a role in the IMT have a period of 98 fs (44) and are related to the V–V dimer stretch. However, the timescale measured here is more consistent with the half period of octahedral V–O–V bending modes at 620 cm^{-1}, which have a period of 55 fs (45). New lattice vibrations could also occur on the excited state potential, which is altered as a result of pump–pulse-induced changes in orbital occupation (24, 28, 46). The process is schematically illustrated in Fig. 4*F*. The resulting displacement can alter the overlap of atomic orbitals and screening,

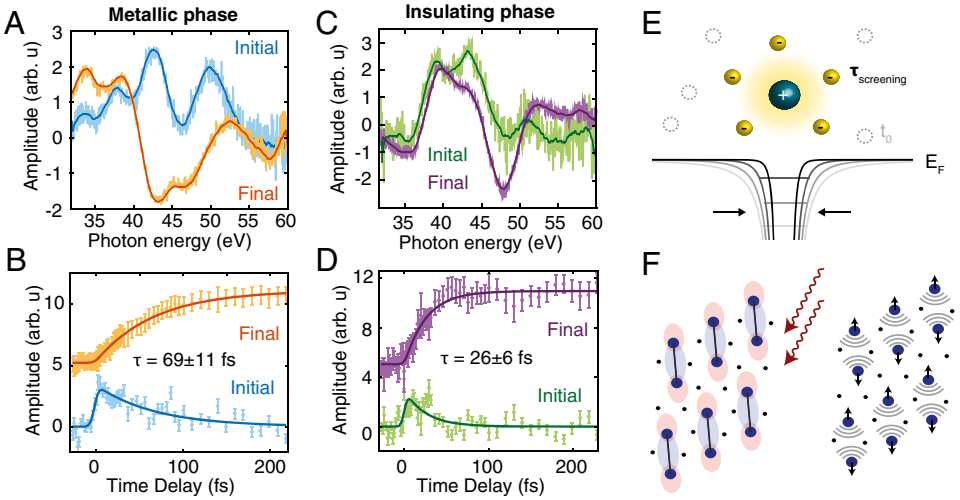

Fig. 4. (*A*) Spectral signatures of the initial (blue) and final (orange) charge distributions observed in the metallic-phase data. Statistical error is apparent from the line fluctuations. The kinetic behavior of each of these spectra in the metallic phase is shown in *B*, where corresponding spectra and kinetics are shown in identical colors. The data points are the result of fitting the ΔOD spectrum at each time delay to a superposition of the two spectral curves in *A*. The results highlight the quality of agreement of the global fit. Analogous spectral and kinetic fit components for the insulating phase are plotted in *C* and *D*, respectively, showing much faster kinetics. *E* illustrates how the phase transition can occur in time as the carriers redistribute spatially to screen the ion cores. The potential well changes from a Coulomb potential (light gray) to a screened Coulomb, or Yukawa potential (dark gray to black), while the horizontal lines represent the binding energy of the d electron, leading up to the Fermi level. *F* illustrates the lattice response, where a change in the excited-state potential energy surface (red: increase, blue: decrease) may trigger impulsive nuclear motion via phonon excitation.

leading to a bandwidth-driven Mott transition (43). While a 1D Peierls-type mechanism has often been discussed, the classical Peierls instability is a feature of d^1 systems (47), whereas VO_2 is determined here to be more accurately d^2. Additionally, the short IMT timescale measured here, which does not align well with vibrational modes typically associated with a Peierls transition (22, 44), lends support to a Mott-like picture.

The timescale measured in this work is consistent with recent femtosecond photoemission (23) and transient reflectivity (25) results on the IMT in VO_2 that yielded 60- and 40-fs (pulse-duration-limited) timescales, respectively, but is not limited by the instrument response function of the measurement. The measurement of a non-pulse-duration-limited 26 ± 6-fs timescale supports a Mott-like mechanism as opposed to Peierls, but does not rule out structural involvement. Electronic and structural effects may indeed be working cooperatively (28). A full theoretical description of the dynamics would likely need to incorporate the electron hopping time, or transfer integral, as well as screening to fully capture the role of both energy shifts and bandwidth changes across the phase transition. The observation of a common nonthermal final state is similar to recent ultrafast pump–probe measurements on the insulating and metallic phases of the prototypical Mott–Hubbard transition in V_2O_3 (48). Further elucidation will require more advanced theory, mapping screening and structural distortion effects onto the XUV spectrum—an exciting and tangible possibility.

The time constant measured here is not necessarily a fundamental lower limit on the timescale of the IMT process in VO_2. It may vary and indeed be faster based on sample crystallinity, doping, strain, and starting temperature (25, 49), as well as on the pulse spectrum and energy of the pump beam, which determines the initial spatial and energy distribution of the injected charges. While all of the previous ultrafast experiments on VO_2 (as well as this work) have used Ti:sapphire laser pulses, the bandwidth and central wavelength of the pulses are varied—however, as most of these results were ultimately limited by the temporal resolution of the experiment, it is not yet possible to map out a trend as to how these factors influence the dynamics. In regard to sample crystallinity, results to date are generally in agreement between single-crystal and polycrystalline films: time-resolved electron diffraction has measured structural timescales in agreement (26, 27), and the fastest electronic timescales measured for each case were previously limited by the pulse duration [<60 fs for thin films (23), and <40 fs for microrods (25)]. We may speculate that excitation closer to the band edge and in single-crystal samples would provide the "natural" speed limit; however, based on this work, dynamics in polycrystalline samples may actually be faster, and more data will be needed to understand this. Broadband XUV attosecond pulses provide access to core-level transitions with temporal resolution on the order of electronic timescales, making FXTAS a powerful tool to study these effects. For VO_2, it is shown that the IMT occurs within 26 ± 6 fs following a change in orbital occupancy. Together with global analysis and theoretical modeling, this methodology has the potential to disentangle the effects of spin, lattice, and orbital degrees of freedom in other correlation-driven phenomena in condensed matter systems.

Materials and Methods

Samples. Experiments were carried out on 25-nm-thick polycrystalline VO_2 thin films prepared by pulsed laser deposition (50) in an Epion PLD-3000 system (base vacuum of 9×10^{-7} torr). A vanadium metal target was ablated at room temperature in an oxygen atmosphere (1.1×10^{-2} torr maintained by 2-ccm flow) by an excimer laser (248 nm, Lambda Physik Comp-Ex 205, nominal pulse duration 25 ns), at a fluence of 4 J/cm^2 with a pulse repetition rate of 25 Hz. The average deposition rate of the VO_x film was 0.3 Å/s. After deposition, the films were annealed in a tube furnace at 450 °C for 10 min in 250 mtorr oxygen to produce stoichiometric VO_2. The samples were deposited on 30-nm-thick freestanding Si_3N_4 membranes provided by Silson Ltd. The clear membrane and sample area was 3 mm × 3 mm, and the membrane was supported on a silicon frame of dimensions 7.5 mm × 7.5 mm.

XUV Measurements. FXTAS was performed in a pump–probe scheme using few-femtosecond carrier-envelope phase-stabilized NIR pump pulses and attosecond probe pulses. Pulses from a Femtopower Compact Pro amplifier were compressed to 5-fs duration and 750-μJ pulse energy using self-phase modulation in a neon-filled (2-bar) hollow-core fiber and a chirped mirror compressor (optics from Ultrafast Innovations). The compressed pulses had a continuous spectrum spanning from 400 to 1,000 nm and were characterized using dispersion scan [Sphere Photonics (51)] to have a duration of 4.9 fs. The 1-kHz repetition rate was reduced to 100 Hz using an optical chopper to avoid sample damage, and the beam was split into two arms using an 80–20% broadband beam splitter.

Probe pulses were generated using the 80% majority arm, by focusing ∼400-μJ 5-fs pulses into a krypton gas target to generate a sub-5-fs attosecond pulse train with a continuous spectrum of XUV light spanning from 30 to 60 eV via high harmonic generation. Residual NIR light from the generation process was removed by transmitting the XUV through a 200-nm-thick aluminum filter. The XUV pulse was focused through the VO_2 sample using a grazing-incidence gold-coated toroidal mirror (ARW Corporation). The 20% pump arm was time-delayed using a retro-reflector on a piezo delay stage with subnanometer positional stability (Physik Instrumente). The pump beam was then focused through the sample collinearly with the probe beam by recombining on a 45° annular mirror, where the pump arm is reflected and the probe arm is transmitted. The NIR beam was focused to ∼200-μm FWHM on the sample, and the XUV beam to ∼60-μm FWHM. After the sample the NIR beam was blocked using a pinhole and a 200-nm aluminum filter. The XUV transmission spectrum through the sample was diffracted using a grazing-incidence variable-line-spacing reflection grating (Hitachi) and recorded on an XUV CCD camera (Princeton Instruments PIXIS). The spectral resolution was determined to be ∼50 meV at 45 eV, calibrated using the linewidths of the $2s^12p^6np$ ($n = 3,4,5\ldots$) Rydberg series of inner-valence excitations in neon (52).

Static absorption spectra were recorded using only the XUV beam and alternating between a sample and a reference target, i.e., a VO_2 sample and a bare Si_3N_4 membrane. The samples were alternated rapidly using fast vacuum translation stages (Physik Instrumente) to compensate for fluctuations and systematic drifts of the high harmonic flux and obtain spectra with sub-1-mΔOD accuracy. Spectra of the metallic phase of VO_2 were obtained by heating the sample in vacuum using a quartz halogen lamp. Samples were checked for uniformity both via optical microscope and by performing a transmission map measurement in the XUV, where the integrated XUV flux was measured as a function of 2D position on the sample surface, and found not to vary by more than ±5%.

Transient absorption spectra were recorded using pump-on/pump-off measurements, where at each time delay a spectrum is saved first with the pump beam switched off and then with the pump beam switched on by means of a computer-controlled optical shutter. This procedure allows spectra to be recorded rapidly back-to-back for higher-quality data. The transient absorption measurements were taken in 2-fs steps from –30 to +30 fs, in 5-fs steps from +30 to +100 fs, and in 10-fs steps from 100 to 220 fs, with a repetition rate of 100 Hz and an exposure time of 1 s. To prevent accumulation of heat in the sample it is critical that subsequent laser pulses do not impinge on the same area of the sample, as heat dissipation in the thin-film samples in vacuum is comparable to the 10-ms inverse laser repetition rate after the optical chopper. To counteract this, the samples were rapidly rotated normal to their surface by mounting the sample in a hollow-shaft motor rotating at 37 ± 3 Hz, and the beam was transmitted at a 0.75-mm radius relative to the motor axis. The material's response in the metallic phase was measured by performing the transient absorption measurement with the heating lamp on as a reference. It was confirmed that without the rotating motor turned on, and using a slower raster-scanning method, where multiple subsequent pump pulses at 100 Hz can impinge on the same spot on the sample before moving to a new area, the samples displayed the dynamic response of the metallic phase. With the spinning motor turned on, the response of the insulating phase could be clearly isolated, evidenced by the absence of any significant signal at negative delays and a qualitatively different measured transient signal. A transient absorption experiment was also performed on a bare Si_3N_4 substrate and it was confirmed that the substrate material was optically transparent and inert to the pump pulses.

Further details can be found in *Supporting Information*. Data are available on request to the corresponding author.

ACKNOWLEDGMENTS. We acknowledge fruitful discussions with Andrey Gandman, Jim Prell, Scott Cushing, Anthony Starace, Miguel Abbate, and Rodrigo Mossanek. This research is supported by Defense Advanced Research Projects Agency PULSE Program Grant W31P4Q-13-1-0017. We also acknowledge support from Multidisciplinary University Research Initiative Grant FA9550-15-1-0037 from the Air Force Office of Scientific Research, and

experimental equipment provided by The Office of the Assistant Secretary of Defense for Research and Engineering through a National Security Science and Engineering Faculty Fellowship grant and the W. M. Keck Foundation and the Department of Energy under Contract DE-AC03-76SF00098. R.E.M. and R.F.H. gratefully acknowledge support from the National Science Foundation (NSF) (DMR-1207507) for the preparation and initial characterization of the VO_2 samples. Portions of this work were performed at the Vanderbilt Institute of Nanoscale Science and Engineering, using facilities renovated under NSF ARI-R2 DMR-0963361. We also gratefully acknowledge a Chancellor's Fellowship for Graduate Study from the University of California, Berkeley (to M.F.J.), an LAM Company Research Fellowship (to M.F.J.), a Feodor Lynen Research Fellowship awarded by the Alexander von Humboldt Foundation (to C.O.), and an Early Postdoc Mobility Fellowship by the Swiss National Science Foundation under Project P2EZP2_165252 (to P.M.K.).

1. Yang Z, Ko C, Ramanathan S (2011) Oxide electronics utilizing ultrafast metal-insulator transitions. *Annu Rev Mater Res* 41:337–367.
2. Krausz F, Stockman MI (2014) Attosecond metrology: From electron capture to future signal processing. *Nat Photonics* 8:205–213.
3. Lorenz M, et al. (2016) The 2016 oxide electronic materials and oxide interfaces roadmap. *J Phys D Appl Phys* 49:433001.
4. Schultze M, et al. (2014) Ultrafast dynamics. Attosecond band-gap dynamics in silicon. *Science* 346:1348–1352.
5. Ramasesha K, Leone SR, Neumark DM (2016) Real-time probing of electron dynamics using attosecond time-resolved spectroscopy. *Annu Rev Phys Chem* 67: 41–63.
6. Cavalieri AL, et al. (2007) Attosecond spectroscopy in condensed matter. *Nature* 449: 1029–1032.
7. Schultze M, et al. (2013) Controlling dielectrics with the electric field of light. *Nature* 493:75–78.
8. Vampa G, et al. (2015) Linking high harmonics from gases and solids. *Nature* 522: 462–464.
9. Mashiko H, Oguri K, Yamaguchi T, Suda A, Gotoh H (2016) Petahertz optical drive with wide-bandgap semiconductor. *Nat Phys* 12:741–745.
10. Tao Z, et al. (2016) Direct time-domain observation of attosecond final-state lifetimes in photoemission from solids. *Science* 353:62–67.
11. Lucchini M, et al. (2016) Attosecond dynamical Franz-Keldysh effect in polycrystalline diamond. *Science* 353:916–919.
12. Wentzcovitch RM, Schulz WW, Allen PB (1994) VO_2: Peierls or Mott-Hubbard? A view from band theory. *Phys Rev Lett* 72:3389–3392.
13. Weber C, et al. (2012) Vanadium dioxide: A Peierls-Mott insulator stable against disorder. *Phys Rev Lett* 108:256402.
14. Biermann S, Poteryaev A, Lichtenstein AI, Georges A (2005) Dynamical singlets and correlation-assisted Peierls transition in VO_2. *Phys Rev Lett* 94:026404.
15. Huffman TJ, et al. (2017) Insulating phases of vanadium dioxide are Mott-Hubbard insulators. *Phys Rev B* 95:75125.
16. Budai JD, et al. (2014) Metallization of vanadium dioxide driven by large phonon entropy. *Nature* 515:535–539.
17. Gray AX, et al. (2016) Correlation-driven insulator-metal transition in near-ideal vanadium dioxide films. *Phys Rev Lett* 116:116403.
18. Aetukuri NB, et al. (2013) Control of the metal-insulator transition in vanadium dioxide by modifying orbital occupancy. *Nat Phys* 9:661–666.
19. Becker MF, et al. (1994) Femtosecond laser excitation of the semiconductor-metal phase transition in VO_2. *Appl Phys Lett* 65:1507–1509.
20. Cavalleri A, et al. (2001) Femtosecond structural dynamics in VO_2 during an ultrafast solid-solid phase transition. *Phys Rev Lett* 87:237401.
21. Cavalleri A, et al. (2005) Band-selective measurements of electron dynamics in VO_2 using femtosecond near-edge x-ray absorption. *Phys Rev Lett* 95:067405.
22. Cavalleri A, Dekorsy T, Chong HHW, Kieffer JC, Schoenlein RW (2004) Evidence for a structurally-driven insulator-to-metal transition in VO_2: A view from the ultrafast timescale. *Phys Rev B* 70:161102.
23. Wegkamp D, et al. (2014) Instantaneous band gap collapse in photoexcited monoclinic VO_2 due to photocarrier doping. *Phys Rev Lett* 113:216401.
24. Wall S, et al. (2012) Ultrafast changes in lattice symmetry probed by coherent phonons. *Nat Commun* 3:721.
25. O'Callahan BT, et al. (2015) Inhomogeneity of the ultrafast insulator-to-metal transition dynamics of VO_2. *Nat Commun* 6:6849.
26. Baum P, Yang D-S, Zewail AH (2007) 4D visualization of transitional structures in phase transformations by electron diffraction. *Science* 318:788–792.
27. Morrison VR, et al. (2014) A photoinduced metal-like phase of monoclinic VO_2 revealed by ultrafast electron diffraction. *Science* 346:445–448.
28. Kübler C, et al. (2007) Coherent structural dynamics and electronic correlations during an ultrafast insulator-to-metal phase transition in VO_2. *Phys Rev Lett* 99: 116401.
29. Suga S, et al. (2009) ~8 keV photoemission of the metal-insulator transition system VO_2. *New J Phys* 11:103015.
30. Henke BL, Gullikson EM, Davis JC (1993) X-Ray interactions: Photoabsorption, scattering, transmission, and reflection at E = 50-30,000 eV, Z = 1-92. *At Data. Nucl Data Tables (NY)* 54:181.
31. De Groot F (2005) Multiplet effects in X-ray spectroscopy. *Coord Chem Rev* 249: 31–63.
32. Zimmermann R, Claessen R, Reinert F, Steiner P, Hüfner S (1999) Strong hybridization in vanadium oxides: Evidence from photoemission and absorption spectroscopy. *J Phys: Condens Matter* 10:5697–5716.
33. Haverkort MW, et al. (2005) Orbital-assisted metal-insulator transition in VO_2. *Phys Rev Lett* 95:196404.
34. Zimmermann R, et al. (1999) Electronic structure of 3d-transition-metal oxides: on-site Coulomb repulsion versus covalency. *J Phys: Condens Matter* 11:1657–1682.
35. Bader SD, et al. (1986) Autoionization in bulk, multilayer, and monolayer Cr. *Phys Rev B: Condens Matter* 33:3636–3643.
36. Davis LC, Feldkamp LA (2012) $M_{2,3}$ spectrum of atomic Mn. *Phys Rev A* 17:2012–2022.
37. Kaurila T, Väyrynen J, Isokallio M (1999) Experimental study of resonant photoemission in the metals V, Cr, Mn and Co. *J Phys: Condens Matter* 9:6533–6542.
38. Van Der Laan G (1991) $M_{2,3}$ absorption spectroscopy of 3d transition-metal compounds. *J Phys: Condens Matter* 3:7443–7454.
39. Shin S, et al. (1990) Vacuum-ultraviolet reflectance and photoemission study of the metal-insulator phase transitions in VO_2, V_6O_{13}, and V_2O_3. *Phys Rev B: Condens Matter* 41:4993–5009.
40. Sayyad S, Eckstein M (2016) Slowdown of the electronic relaxation close to the Mott transition. *Phys Rev Lett* 117:096403.
41. Mott NF (1956) On the transition to metallic conduction in semiconductors. *Can J Phys* 34:1356–1368.
42. Li Y, Luo X, Kröger H (2006) Bound states and critical behavior of the Yukawa potential. *Sci China Phys Mech Astron* 49:60–71.
43. Mott N, Imada M, Fujimori A, Tokura Y (1998) Metal-insulator transitions. *Rev Mod Phys* 70:1039–1263.
44. Yuan X, Zhang W, Zhang P (2013) Hole-lattice coupling and photoinduced insulator-metal transition in VO_2. *Phys Rev B* 88:35119.
45. Wu X, et al. (2016) Influence of infrared optical properties by transformation of the crystal structure in Al-doped vanadium dioxide films. *Opt Mater Express* 6:3500–3506.
46. Zeiger HJ, et al. (1992) Theory for displacive excitation of coherent phonons. *Phys Rev B: Condens Matter* 45:768–778.
47. Peierls R (1991) *More Surprises in Theoretical Physics* (Princeton Univ Press, Princeton).
48. Lantz G, et al. (2017) Ultrafast evolution and transient phases of a prototype out-of-equilibrium Mott-Hubbard material. *Nat Commun* 8:13917.
49. Dönges SA, et al. (2016) Ultrafast nanoimaging of the photoinduced phase transition dynamics in VO_2. *Nano Lett* 16:3029–3035.
50. Nag J, Haglund RF, Jr (2008) Synthesis of vanadium dioxide thin films and nanoparticles. *J Phys Condens Matter* 20:264016.
51. Miranda M, et al. (2012) Characterization of broadband few-cycle laser pulses with the d-scan technique. *Opt Express* 20:18732–18743.
52. Schulz K, et al. (1996) High-resolution experimental and theoretical study of singly and doubly excited resonances in ground-state photoionization of neon. *Phys Rev A* 54:3095–3112.
53. Schilbe P (2002) Raman scattering in VO_2. *Phys B* 316–317:600–602.
54. Wu X, et al. (2016) THz transmittance and electrical properties tuning across IMT in vanadium dioxide films by Al doping. *ACS Appl Mater Interfaces* 8:11842–11850.
55. Gurvitch M, et al. (2007) VO_2 films with strong semiconductor to metal phase transition prepared by the precursor oxidation process. *J Appl Phys* 102:33504.
56. Nag J (2011) The solid-solid phase transition in vanadium dioxide thin films: Synthesis, physics and applications (PhD dissertation, Vanderbilt University, Nashville, TN). Available at etd.library.vanderbilt.edu/available/etd-04202011-182358/. Accessed August 8, 2017.
57. Suh JY, Lopez R, Feldman LC, Haglund RF (2004) Semiconductor to metal phase transition in the nucleation and growth of VO_2 nanoparticles and thin films. *J Appl Phys* 96:1209–1213.
58. Appavoo K, et al. (2012) Role of defects in the phase transition of VO_2 nanoparticles probed by plasmon resonance spectroscopy. *Nano Lett* 12:780–786.
59. Brassard D, Fourmaux S, Jean-Jacques M, Kieffer JC, El Khakani MA (2005) Grain size effect on the semiconductor-metal phase transition characteristics of magnetron-sputtered VO_2 thin films. *Appl Phys Lett* 87:51910.
60. Ott C, et al. (2013) Lorentz meets Fano in spectral line shapes: A universal phase and its laser control. *Science* 340:716–720.
61. Blättermann A, et al. (2015) In situ characterization of few-cycle laser pulses in transient absorption spectroscopy. *Opt Lett* 40:3464–3467.
62. Cavalleri A, et al. (2004) Picosecond soft x-ray absorption measurement of the photoinduced insulator-to-metal transition in VO_2. *Phys Rev B* 69:153106.
63. Wall S, et al. (2013) Tracking the evolution of electronic and structural properties of VO_2 during the ultrafast photoinduced insulator-metal transition. *Phys Rev B* 87:115126.
64. Wegkamp D, Stähler J (2015) Ultrafast dynamics during the photoinduced phase transition in VO_2. *Prog Surf Sci* 90:464–502.
65. Stavitski E, de Groot FMF (2010) The CTM4XAS program for EELS and XAS spectral shape analysis of transition metal L edges. *Micron* 41:687–694.
66. Davis LC, Feldkamp LA (1977) Interaction of many discrete states with many continua. *Phys Rev B* 15:2961–2969.
67. Taguchi M, Uozumi T, Kotani A (1997) Theory of X-ray photoemission and X-ray emission spectra in Mn compounds. *J Phys Soc Jpn* 66:247–256.
68. Berglund CN, Guggenheim HJ (1969) Electronic properties of VO_2 near the semiconductor-metal transition. *Phys Rev* 185:1022–1033.